AGU PUBLICATIONS

JGR

Journal of Geophysical Research: Solid Earth

RESEARCH ARTICLE
10.1002/2016JB013761

Key Points:
- BSR models result in an unusual underestimation of the observed BSR depth along Vestnesa Ridge, in Fram Strait
- Spatial variations in the geothermal gradient and thermogenic gas concentrations control the BSR dynamics in this Arctic setting
- Unconstrained geochemistry of deeper sediments may result in a significant underestimation of the amount of carbons in hydrates

Supporting Information:
- Supporting Information S1

Correspondence to:
A. Plaza-Faverola,
andreia.a.faverola@uit.no

Citation:
Plaza-Faverola, A., S. Vadakkepuliyambatta, W.-L. Hong, J. Mienert, S. Bünz, S. Chand, and J. Greinert (2017), Bottom-simulating reflector dynamics at Arctic thermogenic gas provinces: An example from Vestnesa Ridge, offshore west Svalbard, *J. Geophys. Res. Solid Earth*, *122*, 4089–4105, doi:10.1002/2016JB013761.

Received 17 NOV 2016
Accepted 29 MAY 2017
Accepted article online 1 JUN 2017
Published online 17 JUN 2017

Bottom-simulating reflector dynamics at Arctic thermogenic gas provinces: An example from Vestnesa Ridge, offshore west Svalbard

A. Plaza-Faverola[1], S. Vadakkepuliyambatta[1], W.-L. Hong[1,2], J. Mienert[1], S. Bünz[1], S. Chand[1,2], and J. Greinert[1,3]

[1]CAGE-Centre for Arctic Gas Hydrate, Environment, and Climate, Department of Geosciences, UiT-the Arctic University of Norway, Tromsø, Norway, [2]NGU-Geological Survey of Norway, Trondheim, Norway, [3]GEOMAR-Helmholtz Centre for Ocean Research, Kiel, Germany

Abstract The Vestnesa Ridge comprises a >100 km long sediment drift located between the western continental slope of Svalbard and the Arctic mid-ocean ridges. It hosts a deep water (>1000 m) gas hydrate and associated seafloor seepage system. Near-seafloor headspace gas compositions and its methane carbon isotopic signature along the ridge indicate a predominance of thermogenic gas sources feeding the system. Prediction of the base of the gas hydrate stability zone for theoretical pressure and temperature conditions and measured gas compositions results in an unusual underestimation of the observed bottom-simulating reflector (BSR) depth. The BSR is up to 60 m deeper than predicted for pure methane and measured gas compositions with >99% methane. Models for measured gas compositions with >4% higher-order hydrocarbons result in a better BSR approximation. However, the BSR remains >20 m deeper than predicted in a region without active seepage. A BSR deeper than predicted is primarily explained by unaccounted spatial variations in the geothermal gradient and by larger amounts of thermogenic gas at the base of the gas hydrate stability zone. Hydrates containing higher-order hydrocarbons form at greater depths and higher temperatures and contribute with larger amounts of carbons than pure methane hydrates. In thermogenic provinces, this may imply a significant upward revision (up to 50% in the case of Vestnesa Ridge) of the amount of carbon in gas hydrates.

1. Introduction

Gas hydrates are crystalline structures in which gas molecules are trapped in water cages. They form under low temperature and high pressure in marine and permafrost sediments where a sufficient supply of methane exists [e.g., *Kvenvolden and Claypool*, 1988]. Gas hydrates may also exist as unwanted blocking precipitates in gas pipelines. In nature, gas hydrates host substantial amounts of carbon (i.e., 10^2–10^6 Gt) [*Dobrynin*, 1981; *Soloviev*, 2002] and the associated gas (mainly methane) is considered as an untapped energy resource but is also seen as a potential global warming amplifier if methane gas reaches the atmosphere [e.g., *Moridis et al*., 2013]. In addition, gas hydrates are discussed as trigger for geohazards as their destabilization is inferred to increase slope instability or fluid flow [e.g., *Sultan et al*., 2004]. A commonly observed indicator of gas hydrate occurrence in sediments is the bottom-simulating reflector (BSR), a high-amplitude seismic reflection that crosscuts stratigraphic layers and mimics the seafloor but with an opposite seismic amplitude polarity [e.g., *Mienert and Bünz*, 2016]. The gas hydrate stability zone (GHSZ) represents the interval where gas hydrates are theoretically stable; its boundaries are defined by pressure-temperature (P-T) conditions, salinity of the pore fluid, and the source gas composition [*Sloan and Koh*, 2008]. The BSR is observed at or nearby the base of the gas hydrate stability zone (BGHS) in response to the acoustic impedance contrast between hydrate bearing and underlying gas bearing sediments [*MacKay et al*., 1995; *Shipley et al*., 1979; *Xu and Ruppel*, 1999].

The dynamics of a gas hydrate system at a specific geological setting in response to dominant external factors such as bottom water temperature (BWT), geothermal gradient (GTG), heat flow, pressure, gas composition, and salinity can be assessed by analyzing discrepancies between the predicted BGHS and the observed BSR [e.g., *Bale et al*., 2014; *Liu and Flemings*, 2011; *Ruppel*, 1997; *Xu and Ruppel*, 1999]. For instance, in convergent margin settings such as Nankai Trough and the Hikurangi Margin, the depth of the BSR (300–500 m below seafloor (mbsf)) readjusts primarily to heat flow changes and pressure changes due to uplift and erosion [*Kinoshita et al*., 2011; *Pecher et al*., 2005], whereas in continental slopes along passive margins, seafloor temperature variability and sea level cycles can be major factors controlling the BSR depth [e.g., *Berndt et al*., 2014;

Mienert et al., 2005; *Skarke et al*., 2014; *Westbrook et al*., 2009]. Another factor suggested to influence the BSR depth is the capillary effect which allows gas to coexist with hydrates in sediments right above and below the BGHS. This can shift the BSR a few meters above the theoretical BGHS [*Liu and Flemings*, 2011], reconciling common worldwide observations of a shallower BSR than theoretical predictions [e.g., *Liu and Flemings*, 2011; *Ruppel*, 1997; *Torres et al*., 2008].

Global estimates of gas hydrate concentrations rely on the prediction of the extent of the GHSZ at specific geological settings [e.g., *Klauda and Sandler*, 2005]. The GHSZ extent can be predicted using thermodynamic models [e.g., *Bale et al*., 2014; *Dickens and Quinby-Hunt*, 1994; *Lu and Sultan*, 2008; *Sloan and Koh*, 2008] together with constraints from direct sampling and indirect evidence from both geophysical and geochemical data. Several numerical models have been proposed that emphasize controls on hydrate stability by specific parameters [*Bale et al*., 2014, and references therein; *Peszynska et al*., 2016]. The modeling approach by *Sloan and Koh* [2008] is particularly widely implemented for hydrate studies in different continental settings due to its applicability for gas hydrates with a mixed composition of microbial and thermogenic methane with higher-order hydrocarbons (i.e., structures I, II, and H). Essentially, the gas source for hydrates in continental margins can be a mixture of microbial methane, thermogenic methane, and larger hydrocarbons such as ethane and propane, or even abiogenic gas [*Johnson et al*., 2015; *Rajan et al*., 2012]. The presence of ethane, propane, and butane in addition to methane is a critical factor influencing hydrate stability and thus the thickness of the GHSZ, particularly in margins with structural focusing of hydrocarbons [e.g., *Milkov and Sassen*, 2002; *Paganoni et al*., 2016]. Gas hydrates with larger guest molecules such as ethane are more stable and form in wider P-T regimes if compared to pure methane hydrate [*Sloan and Koh*, 2008]. Except for active fault-controlled seepage systems (e.g., at the Gulf of Mexico and Caspian Sea) where thermogenic gas is transported to the seafloor [*Brooks et al*., 1984; *Ginsburg et al*., 1992], gas samples in hydrate systems commonly show >99% microbial methane in their composition [*Kvenvolden and Lorenson*, 2001].

In situ thermogenic gas hydrate accumulations have been often considered as "anecdotal exceptions" [*Sloan and Koh*, 2008]. Thus, a common heuristic to simplify predictions of the GHSZ thickness and global hydrate inventories has been that seafloor gas compositions of ~100% methane is representative for the entire thickness of the GHSZ. However, our knowledge about gas hydrate systems from field observations is growing and the number of documented hydrate provinces with thermogenic gas input is steadily increasing—e.g., offshore Northern California [*Kvenvolden and Field*, 1981], the Gulf of Mexico [*Brooks et al*., 1984], the Cascadia Margin [*Lu et al*., 2007], the Barents Sea [*Chand et al*., 2008], Lake Baikal [*Khlystov et al*., 2013], the Alaska North Slope [*Pinero et al*., 2014], the west Svalbard margin [*Smith et al*., 2014], and the continental slope of Sabah [*Paganoni et al*., 2016]. The significance of higher-order hydrocarbons contributing to the carbon budget, although not necessarily predominant at the near surface sediments, has thus become more evident. Essentially, 1 m^3 of ethane (C_2H_6) hydrate contains 2 times the amount of carbon compared to a similar volume of methane (CH_4) hydrate. These higher-order hydrocarbon hydrates in nature remain a less understood component of gas hydrate systems.

Using constraints from integrated geophysical and geochemical data, this study implements the gas hydrate phase boundary by *Sloan and Koh* [2008] to investigate the effect of higher-order hydrocarbons on the dynamics of a well-defined BSR. The study focuses on a deep marine (>1000 m water depth) gas hydrate system located between the western continental slope of Svalbard and the Arctic mid-ocean ridges (Figure 1). The paper documents a field example where the BSR dynamics, in addition to spatial changes in the geothermal gradient, is likely influenced by laterally and vertically variable gas compositions and concentrations. The study emphasizes that near-surface headspace gas compositions are not necessarily representative of gas compositions deeper in the sediment. Our findings suggest that the underestimation of the GHSZ thickness due to an unconstrained pure methane-hydrate assumption may be noteworthy, particularly in regions with significant input from thermogenic gas reservoirs (e.g., the Arctic). Such findings may have implications for refining global estimates of gas hydrates as major carbon capacitors and their interplay with past and present climate.

2. The Study Area: Vestnesa Ridge

Vestnesa Ridge is a sediment drift developed on <19 Ma old oceanic crust [*Engen et al*., 2008; *Hustoft et al*., 2009; *Johnson et al*., 2015] in water depths around 1000 m (Figure 1). It is located offshore west Svalbard, with its westernmost end descending toward the Molloy spreading ridge (Figure 1a). The stratigraphy of the

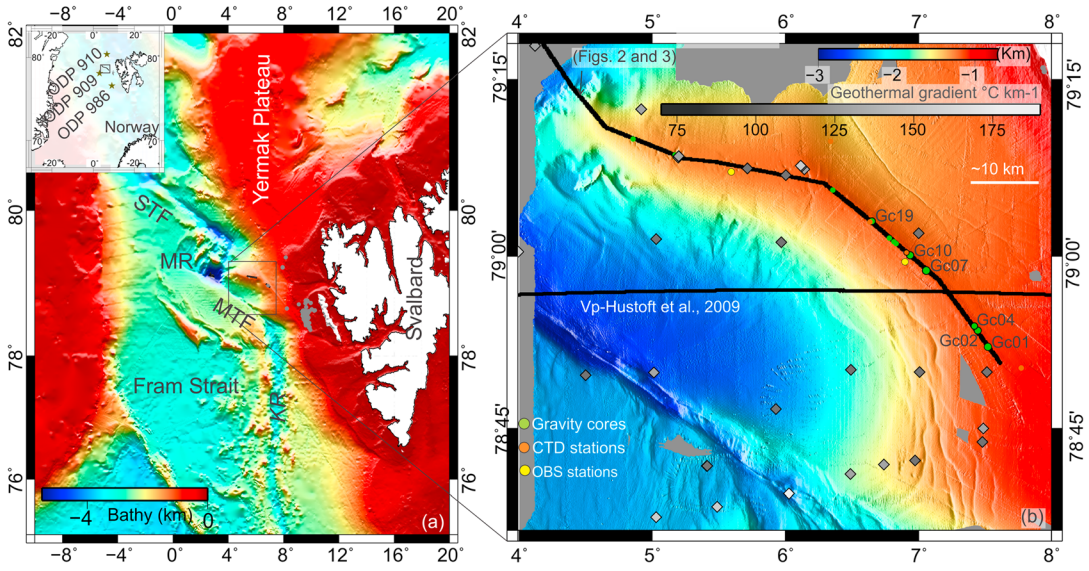

Figure 1. (a) Location of Vestnesa Ridge offshore the west Svalbard margin. Vestnesa Ridge is bounded by the Molloy Ridge (MR) to the west, the Spitsbergen and the Molloy transform faults (MTF and STF) to the north and south, respectively, and by the west Svalbard continental margin to the east. The inset indicates the location of sites from the Ocean Drilling Program (ODP) in the region. (b) Multibeam bathymetry of Vestnesa Ridge and data collected. Regional heat flow is from *Crane et al.* [1991]. Ocean bottom seismometer (OBS) stations used by *Petersen et al.* [2010] and *Goswami et al.* [2015] are projected.

sediment drift consists of three main units [*Eiken and Hinz*, 1993; *Hustoft et al.*, 2009] interpreted on our seismic data based on correlation with Ocean Drilling Program (ODP) Leg 151, Sites 910–912 located on the Yermak Plateau (YP) north of Vestnesa Ridge [*Mattingsdal et al.*, 2014; *Plaza-Faverola et al.*, 2015]. YP-1, the oldest (Miocene) sequence, is characterized by synrift deposition directly over oceanic crust, YP-2 is dominated by sediments deposited by contour currents and has a main depocenter parallel to the passive west Svalbard margin, and YP-3 consists of glaciomarine sediments and turbidites mainly toward the easternmost segment of the ridge. The YP-2/YP-3 boundary is estimated to be ~2.7 Ma. It marks the intensification of the Northern Hemisphere glaciation in the region [*Mattingsdal et al.*, 2014]. The GHSZ along the ridge is within the YP-3 sequence. More precisely, the base of the GHSZ toward the shallowest end of Vestnesa Ridge lies ~90 m below a distinct seismic horizon (Figures 2 and 3) correlated with a 1.5 Ma old stratigraphic interface [*Plaza-Faverola et al.*, 2015]. This stratigraphic period has been suggested to mark the onset of local glacial intensification at the Yermak Plateau [*Mattingsdal et al.*, 2014]. Except for vertical disturbances caused by gas chimneys and fine-scale faults (i.e., few tens of meters), main stratigraphic interfaces extend undisturbed along ~100 km long Vestnesa Ridge, suggesting a homogenous, largely invariant stratigraphic setting.

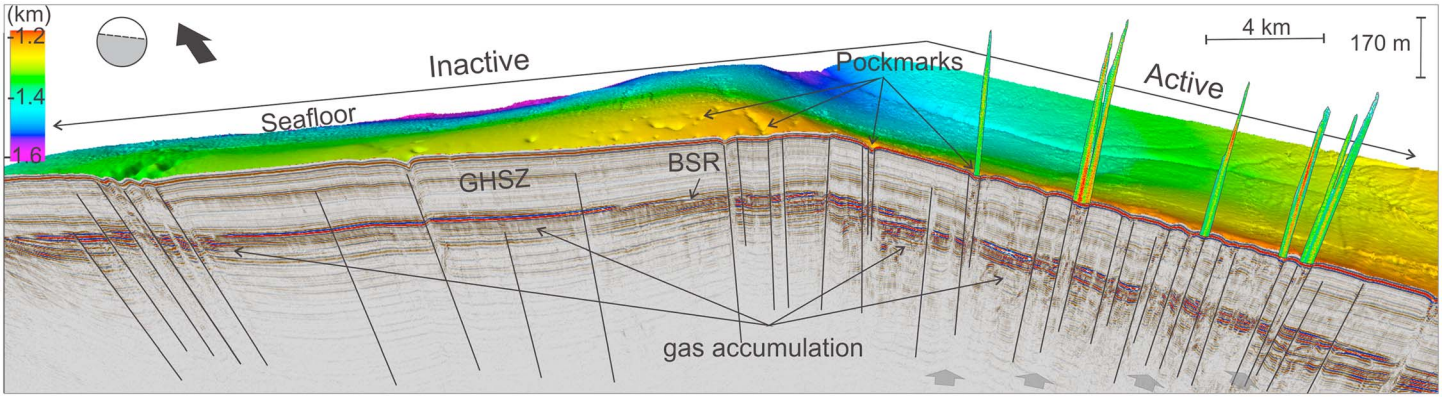

Figure 2. Three-dimensional composite figure of Vestnesa Ridge gas hydrate system: the seismic profile shows faults piercing through the gas hydrate stability zone and expected active fluid pathways (arrow), the bathymetry data show the character of seafloor pockmarks, and echosounder data show active seepage sites where gas bubbles form acoustic flares have been identified so far.

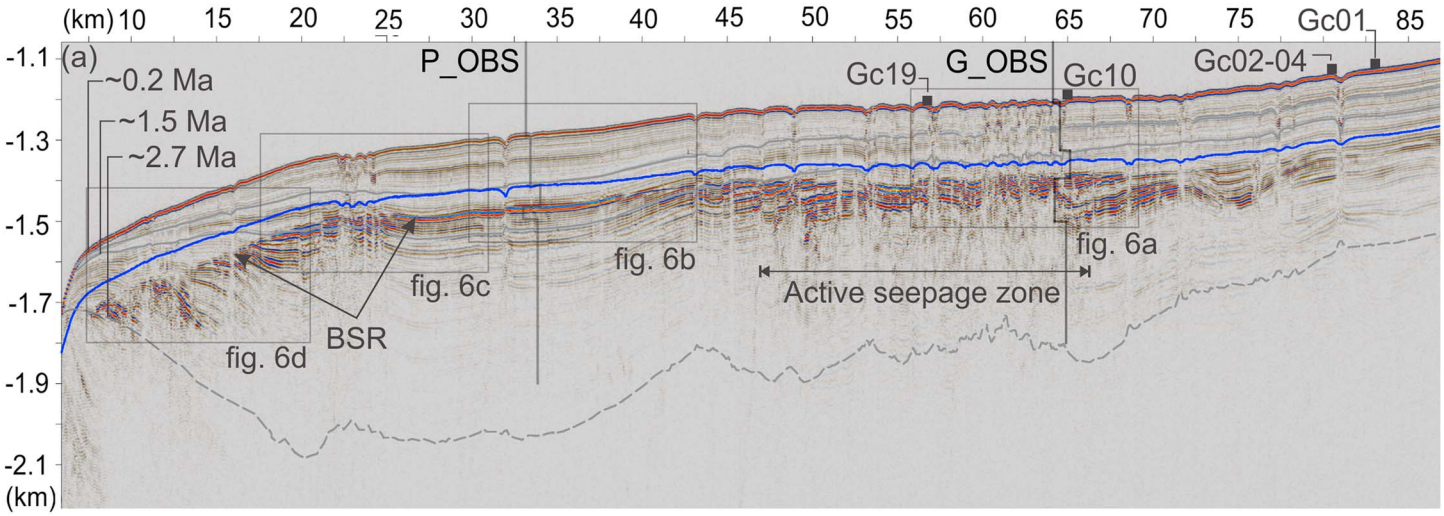

Figure 3. Seismic transect along Vestnesa Ridge in depth. Seismic velocities used for depth conversion are from ocean bottom reflection seismic stations (P_OBS and G_OBS) [*Goswami et al.*, 2015; *Petersen et al.*, 2010]. BSR stands for bottom-simulating reflector. Gas samples from five gravity cores along the ridge (GC01, GC02, GC04, GC10, and GC19) were used for modeling the base of the gas hydrate stability zone (BGHS). The predicted BGHS for pure methane (blue) projects up to 60 m shallower than the observed BSR.

Geothermal gradients along the ridge are considerably higher (i.e., >80°C km^{-1}; Figure 1) than toward the continental margin [*Crane et al.*, 1991; *Sundvor et al.*, 2000; *Vogt et al.*, 1999]. Fluid escape-related pockmarks at the seafloor were first identified in the 1990s along the entire ridge extent [*Vogt et al.*, 1994]. Gas chimneys have been documented associated to the pockmarks [*Bünz et al.*, 2012; *Hong et al.*, 2016; *Petersen et al.*, 2010], but present-day seepage is restricted to the southeastern part of the ridge [Figure 2; *Bünz et al.*, 2012; *Hustoft et al.*, 2009]. Three-dimensional seismic data document the presence of fine-scale faults and fractures controlling the distribution of gas chimneys, suggesting a tectonic control on seepage activity along the ridge for at least the last 2.7 Ma [*Plaza-Faverola et al.*, 2015]. Thermogenic gas was first identified in hydrate samples from an active pockmark with associated hydrate-coated gas bubbles that reached the upper limit of the GHSZ in the water column at ~400 m below sea surface [*Smith et al.*, 2014]. The 1-D petroleum system modeling suggests that organic-rich Miocene and potential Eocene source rocks caused thermogenic methane production within given temperature and burial conditions near the ridge [*Dumke et al.*, 2016]. In addition to thermogenic gas, abiogenic gas from mantle serpentinization was recently suggested to sustain hydrate accumulations at the western flank of the active Knipovich spreading ridge [*Johnson et al.*, 2015].

3. Data and Methods

3.1. Seismic Data

An acoustic survey and gas sampling program were conducted on board R/V *Helmer Hanssen* during CAGE_1 cruise in 2013 to investigate gas hydrate system dynamics at Vestnesa Ridge. We used high-resolution seismic data (20–300 Hz) to map the BSR along the crest of the ridge (Figures 2 and 3). The 2-D seismic lines were acquired with the P-Cable seismic equipment [*Planke et al.*, 2009] configured for 2-D surveys. The length of the streamer was 100 m providing 32 recording channels. The minimum nominal offset was 50 m and maximum offset 150 m. The source consisted of two GI-Guns configured as 45/45 and 45/105 cm^3. The sampling rate was 0.5 ms, and the shooting interval is 10 s at an average sailing speed of 4.5 knots. Processing included band-pass filtering and Stolt migration at a constant *P* wave velocity of 1500 m/s.

The seismic traces have a dominant frequency of ~80 Hz. The theoretical lateral resolution after migration is given by a binning size of 6.25 m. The theoretical vertical resolution is ~4.5 m at the seafloor, calculated as $\lambda/4$ using a water velocity of 1469 m s^{-1}.

3.2. Headspace Gas Samples

Gas compositions used for BGHS predictions were obtained by analyzing the dissolved gas concentrations in pore water samples from gravity cores along Vestnesa Ridge (Table 1). After splitting of the cored sediments

Table 1. Gas Concentrations Measured in Pore Water Samples From Gravity Core (GC) Stations Used for Modeling of the Gas Hydrate Stability Zone

Core Station	C_1(%)	C_2(%)	C_3–C_6(%)
100% CH_4	100	0	0
GC19	95.62	2.06	2.32
GC10	99.56	0.34	0.1
GC04	95.04	2.13	2.82
GC02	98.39	0.71	0.89
GC01	93.50	3.10	3.40

in meter sections, 3 mL of sediment was subsampled by cutoff syringes and stored in 20 mL glass vials with 9 mL of saturated NaCl solution. The vials were crimped sealed with rubber stoppers and aluminum caps and stored in a dark room at ~+3.6°C.

Hydrocarbon gases concentrations were analyzed by a ThermoScientific FOCUS gas chromatogram (GC) equipped with a flame ionization detector (temperature ramping 40, 70, and 120°C; H_2 carrier gas, Resteck 2 m packed column HS-Q 80/100). Accuracy of the method and system is 5% for methane and 8% for ethane and propane. Stable carbon isotope ratios of methane (Table S1 in the supporting information) were determined by using a continuous flow gas chromatography-isotope ratio mass spectrophotometer. Methane and ethane were separated in a Thermo Trace GC (Isotherm at 70°C, He-carrier gas, ShinCarbon 1.5 m packed column). The subsequent conversion of methane and ethane, respectively, to carbon dioxide was conducted in a Ni/Pt combustion furnace at 980°C. The $\delta^{13}C$ value of produced CO_2 was determined by isotope ratio mass spectrometry (Thermo MAT253). Reproducibility of stable carbon isotope determination is ±0.3‰. All isotope ratios are given in the δ notation versus Vienna Peedee belemnite standard. Isotope ratios and gas compositions are reported as averages from three samples, which agreed well with each other.

3.3. Gas Hydrate Stability Zone Modeling

The observed BSR depth was compared to the predicted BGHS for 100% methane gas hydrate and five measured gas compositions (Figure 1). Theoretical predictions of the BGHS were made using the CSMHYD program's P-T phase boundary curves for hydrates with mixed gas compositions [*Sloan and Koh*, 2008]. The program uses an algorithm based on Gibbs energy minimization and calculates multiphase equilibria for any given temperature or pressure. We implemented the program such as it calculated pressure for given temperature values. In deep water settings, these pressure values have a mathematical uncertainty of ~15% (Table 2) [*Sloan and Koh*, 2008]. Pressure estimations (P) were converted to depths (h) as $h = P/(\rho \times g)$, where ρ (1030 kg m^{-3}) and g (9.8 m s^{-2}) are water density and acceleration due to gravity, respectively. Pressure was assumed to be hydrostatic and a pore water salinity of 35 g L^{-1} was used in our models.

Resulting temperature-depth profiles were compared with the thermal profile from conductivity-temperature-depth (CTD) data and geothermal gradient at each location (~6.5 m spatial interval) along the seismic transect. If the temperature from theoretical stability curves at a particular depth was greater than that from field data, hydrates were deemed to be stable at that depth.

Bottom water temperatures along the ridge were constrained by historical CTD casts (1960–2013) [*National Oceanographic Data Center*, 2013] showing a negligible regional fluctuation of ±0.1°C over the last 50 years. For constraining GTG used in the models we considered available regional values measured in situ using up to 10 m long temperature probes with an associated instrumental error of ±10°C km^{-1} [*Crane et al.*, 1991; *Sundvor et al.*, 2000; *Vogt et al.*, 1999]. GTG along Vestnesa Ridge increases westward from ~80 ± 10°C km^{-1} at the eastern end of the ridge to ~180 ± 10°C km^{-1} toward the Molloy Deep, an ultraslow spreading ridge [*Crane et al.*, 1991; *Sundvor et al.*, 2000; *Vogt et al.*, 1999].

Table 2. Model Parameters, Used Values for Final Models of the BGHS for Specific Gas Compositions and Associated Uncertainty Values Considered for the Uncertainty Analysis

Parameter	Value	Uncertainty
Water depth (m)	1099–2913	±5
Bottom water temperature (°C)	−0.896–0.793	±0.1
Geothermal gradient (^oC km^{-1})	85–180	±10
Pore water salinity (g L^{-1})	35	±35
Pressure (CSMHYD) (%)	-	±15

Uncertainties in predicted BGHS depths were estimated by statistically combining uncertainty ranges of individual parameters (Table 2 and supporting information Figure S2). Overall, the predicted BGHS has a mean standard deviation (-1σ) of 18 m over the seismic profile (for pure methane) due to the

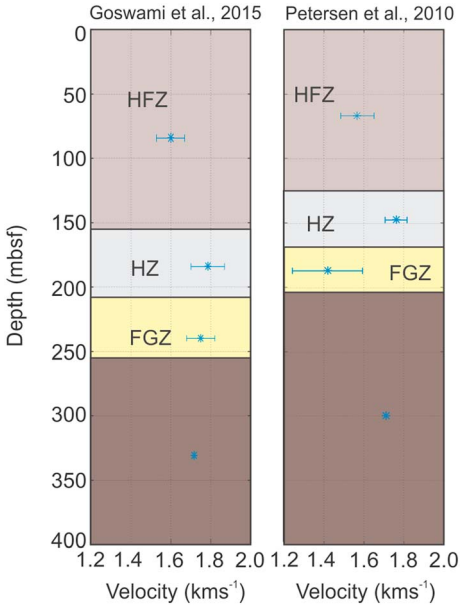

Figure 4. *P* wave velocity (*Vp*) models extracted from *Petersen et al.* [2010] and *Goswami et al.* [2015] with estimated uncertainties (1σ). Four seismic velocity layers are used in addition to the water column velocity to depth convert the seismic section. The upper layer, showing a normal trend of *Vp*, is referred to as the hydrate free zone (HFZ); a zone showing slightly anomalous higher velocities in both models is referred to as the hydrate zone (HZ); a zone of anomalous inverted *Vp* corresponds to the free gas zone (FGZ). The observed bottom-simulating reflector (BSR) is in good agreement with the interface between the HZ and the FGZ in both OBS-derived *Vp* models.

combined effect of uncertainties in BWT, GTG, pore water salinity, seafloor depth, together with the mathematical uncertainty associated with CSMHYD (Table 2). The uncertainties related to *Sloan and Koh*'s [2008] approach seems to be the major contributor to the errors, which is highest at shallower water depths (up to 26 m toward the east end of the transect) and lowest at deeper water depths (up to 12 m toward the west end of the transect).

3.4. Time to Depth Conversion of the Seismic Profile

Predicted BGHS for measured gas compositions were compared with the BSR picked on seismic data converted to depth. The accuracy of the comparison between modeled and observed BSR depends on well-constrained velocities used for depth conversion. Stretching the two-way travel times of seismic records to depth is equivalent to solving the forward modeling problem. This is to find *P* wave velocities (*Vp*) and layer thicknesses that explain the recorded travel times. The depth (*d*) of a seismic reflector is proportional to one-way travel time (*t*) and velocity (*v*) through the relationship $d = t \times v$. Hence, the higher the seismic velocities, the deeper the BSR in the depth section. In a depth converted seismic profile using the water column velocity the BSR appears toward its minimum probable depth.

Along Vestnesa Ridge we have interval velocity constraints from ocean bottom seismometers (OBSs). We used *P* wave interval velocity information from two OBSs located >20 km apart from each other along the ridge [*Goswami et al.*, 2015; *Petersen et al.*, 2010]. Velocity models from these two sites document a velocity increase from ~1470 m/s at the seafloor to ~1800 m/s at the BSR (Figure 4) and are in good agreement with a third velocity model from multichannel seismic intersecting the eastern segment of Vestnesa Ridge [*Hustoft et al.*, 2009]. We used velocities constrained by these two OBS-derived 1-D models for four layers in addition to the water column [Figure 4; *Goswami et al.*, 2015; *Petersen et al.*, 2010]. The extent of the four layers are delineated in the velocity models by their characteristic velocities and are denoted for simplicity as hydrate-free zone (HFZ), hydrate zone (HZ), free gas zone (FGZ), and deeper layers (Figure 4). In each layer, the available interval velocities from the two velocity models are averaged, resulting in interval velocities with associated standard deviations (1σ). The BSR represents the interface between the zone of slightly anomalous higher velocities above (HFZ) and anomalous low velocities underneath corresponding to a zone of free gas in the sediments (FGZ) [*Goswami et al.*, 2015; *Petersen et al.*, 2010].

To constrain the range of variation of the BSR depth with changing velocities, we depth converted our seismic line using six velocity functions derived from the two 1-D velocity models [*Goswami et al.*, 2015; *Petersen et al.*, 2010] including the lower and upper boundaries of the standard deviations (1σ) for each model. The combined effect of these velocity uncertainties results in ±8 m error (~4–6% of the total GHSZ thickness) in the observed (mapped) BSR depth (Figure 5, shaded blue area).

The stratigraphy in the upper strata is largely invariable along the ridge (Figure 3). Hence, we have no reasons to suspect a significant effect of lateral velocity variations on the BSR depth. Slight differences in the interval velocities reported by the two OBS sites at comparable depths [*Goswami et al.*, 2015; *Petersen et al.*, 2010] may

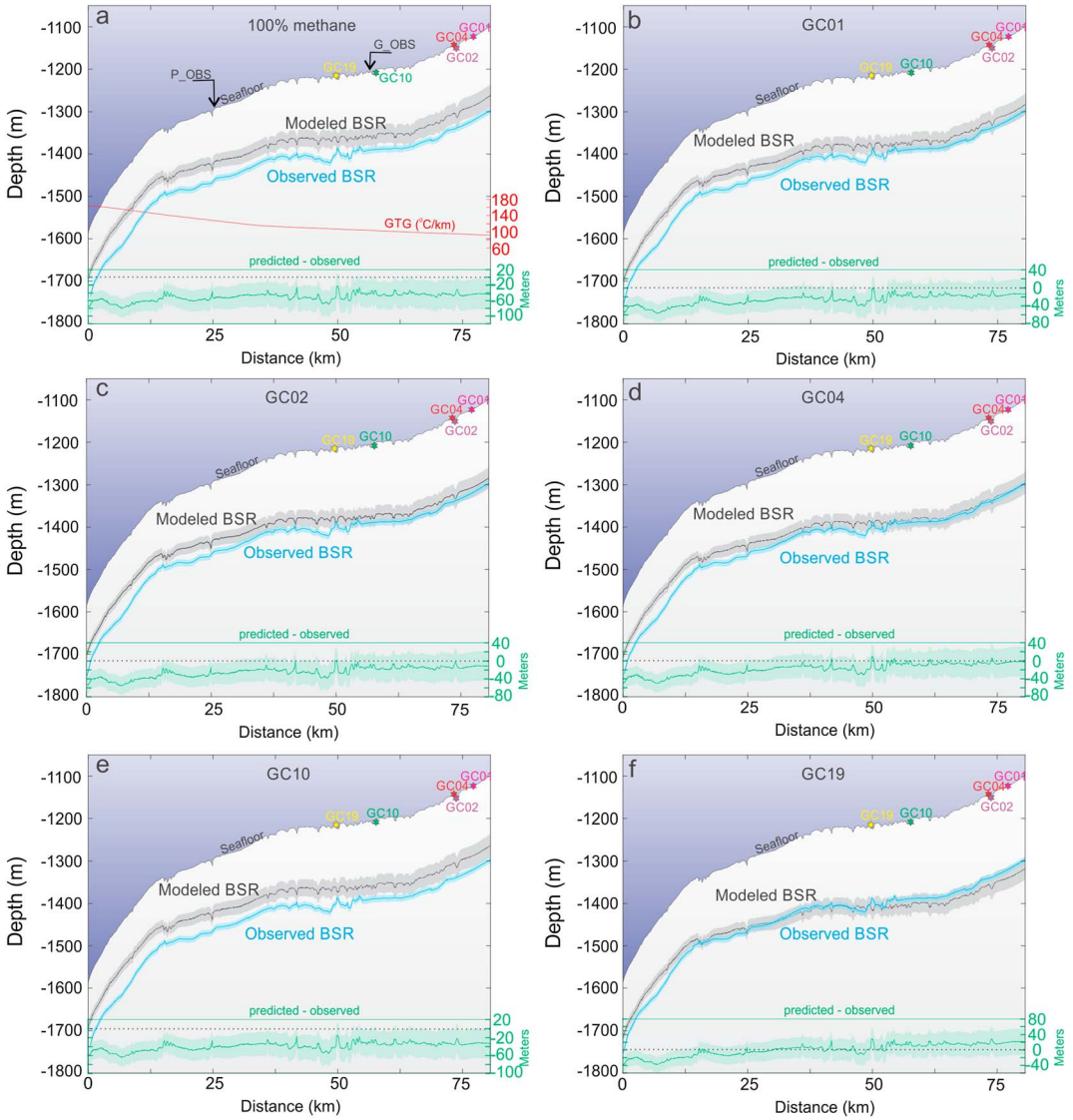

Figure 5. Comparison between observed (blue solid line) and modeled (gray solid line) BSR depths within uncertainty ranges (shaded areas), for pure methane and measured gas compositions from gravity cores G01, G02, G04, G10, and G19 along Vestnesa Ridge. The mismatch between models and observation (green solid line) is also presented with a range of uncertainty associated (green shaded envelop) which results from comparisons of minimum and maximum scenarios bounded by model and depth conversion uncertainties. The regional trend of the geothermal gradient (red) shows a lateral increase of ~100°C km^{-1} from one end to the other along the ~120 km long seismic profile.

be partially due to differences in the picked reflections for the base of the layers. In addition, small focused accumulations of faster or lower seismic velocity material (e.g., gas hydrates or carbonates and free gas respectively) inside gas chimneys or above the BSR may result in small scale but focused lateral velocity variations. Nevertheless, if gas hydrate or carbonate bearing layers is hypothetically abundant within the entire GHSZ beyond the resolution of the OBS models, the BSR depth would be deeper than assumed. Regionally, the BSR depth in our depth-converted transect provides an excellent match for that in *Petersen et al.* [2010] and *Goswami et al.* [2015] at the location of the OBS sites (Figure 4).

4. Results: The Observed BSR and Predicted BGHS Along Vestensa Ridge

A continuous BSR along Vestnesa Ridge marks the top of a >30 m thick high-amplitude, low-velocity zone indicative of free gas [*Hustoft et al.*, 2009]. The BSR depth decreases from ~195 ± 8 m bsf at 1093 m water depth, to ~140 ± 8 m bsf where Vestnesa Ridge approaches the Molloy spreading ridge (>1500 m water

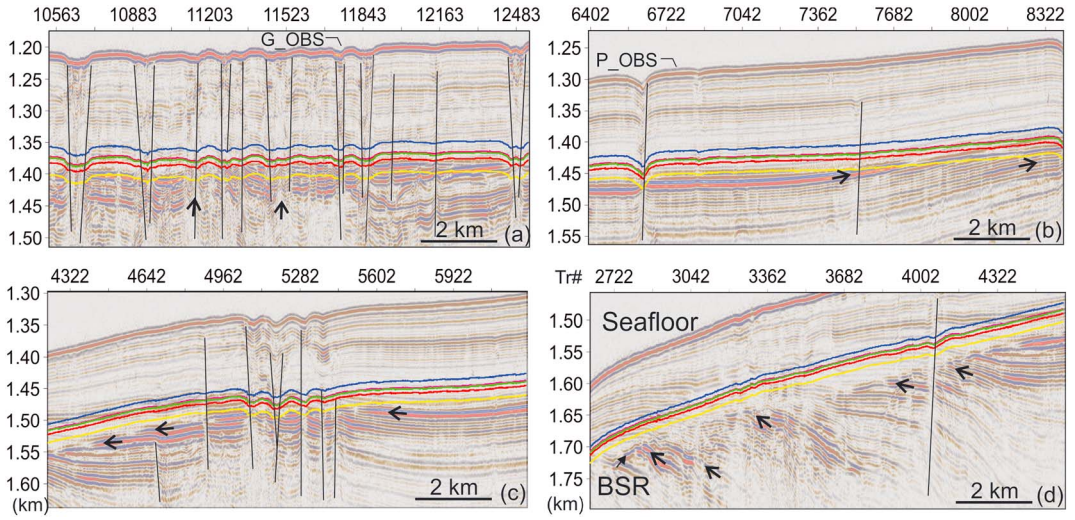

Figure 6. (a–d) Magnified view of key zones along Vestnesa Ridge where distinct mismatch between the BSR depth and predicted BGHS indicate spatial variations in the BSR dynamics. The models are projected: pure methane (blue), GC01 (pink), GC02 (purple), GC04 (red), GC10 (green), and GC19 (yellow).

depth; Figure 5). Such a decrease of >40 m in the BSR depth, despite a larger water column and thus increase in hydrostatic pressure, reflects the regional effect of an increasing geothermal gradient from ~80°C km^{-1} to ~180°C km^{-1} toward the Molloy spreading ridge (Figures 1 and 5). The regional trend of the GTG experiences a lateral increase of ~100°C km^{-1} from one end to the other of the investigated seismic profile (Figure 5). The BSR generally follows the seafloor morphology except locally at gas chimneys, where a clear BSR does not exist. Toward Molloy Ridge, the BSR experiences a gentle downward bend with respect to the seafloor (Figures 5 and 6d).

We modeled the BGHS for five gas compositions (Table 1) in addition to a gas concentration of 100% methane. Gas analyses were accomplished along the easternmost segment of Vestnesa Ridge (Figure 1), and the samples show variable amounts of higher-order hydrocarbons. From east to west the gas samples are (Figures 1, 3, and 5) as follows: GC01—located at the eastern boundary of a zone with active pockmarks along the ridge, GC02 and GC04—located at the flank of a pockmark that is inactive (no gas bubbles documented) at present, and GC10 and GC19—located at the flanks of active pockmarks. While GC10 shows ~99% methane, the other samples show >2% ethane and higher-order hydrocarbons. GC04 shows the highest concentration of ethane and propane (Table 1).

Comparison of the predicted BGHS for each seafloor gas sample with the observed BSR indicates that the BSR depth is generally underestimated by the models beyond the uncertainty ranges (Figure 5). The BSR is in average 40–60 m deeper than the predicted BGHS for pure CH_4 (Figure 5a) and for GC10 (99.56% CH_4) (Figure 5e). The best fitting model is the BGHS for GC19 (i.e., with ~4% ethane and higher hydrocarbons) which shows an average mismatch ranging from +20 (the BSR is shallower than predicted) around the active seepage segment of Vestnesa Ridge to −35 m (the BSR is deeper than predicted) toward the Molloy Ridge (Figure 5f). The other four gas compositions result in a BGHS that lies between the BGHS for pure methane and that for GC19 (Figures 5b–5e), depending on the amount of propane in the samples. At the location of gas samples GC19 and GC04, the misfit between predicted BGHS for their corresponding gas compositions and the BSR is almost zero (Figures 5d and 5f). Near GC01 and GC02 the misfit is within the model uncertainties. Overall, the BGHS for gas concentration in GC19 fits the observed BSR within the uncertainty range along most of Vestnesa Ridge except for the westernmost 20 km of the transect. Here the discrepancy becomes more prominent (i.e., up to 30 m) and corresponds with the zone of downward bending BSR (Figure 6).

5. Discussion

In continental margins, the BSR coincides with the BGHS when the gas input into the GHSZ reaches a critical value leading to the formation of gas hydrates right at the base of the GHSZ [e.g., *Haacke et al.*, 2008; *Xu and*

Ruppel, 1999]. In low-methane flux systems like Blake Ridge, discrepancies between the BSR and the BGHS have been observed and attributed to the presence of a transition zone without significant amounts of hydrates or free gas [*Xu and Ruppel*, 1999]. However, at structurally controlled systems with high-methane flux (e.g., Hydrate Ridge) drilling through the BSR has shown that the BSR does coincide with the predicted BGHS [*Trehu et al*., 2004]. Similarly, a recent study from borehole data at thermogenic gas hydrate systems of the convergent margin of Borneo documents a BSR that coincides with the BGHS predicted for measured concentrations of >96% methane type II gas hydrates [*Paganoni et al*., 2016].

Under the assumption that the BSR indicates the base of the GHSZ at Vestnesa Ridge, we interpret the discrepancies between modeled and observed BSR as indicative of a highly dynamic gas hydrate system that is structurally controlled and under the influence of mid-ocean ridge thermal regimes. There are clear differences in the fluid flow systems developed at the eastern and western Vestnesa Ridge segments as indicated by the distribution of active gas chimneys and fault structures [*Plaza-Faverola et al*., 2015]. These differences are also reflected in how the BSR compares with the models (Figure 5) and suggest that diverse factors influence the BSR dynamics at key zones along Vestnesa ridge.

5.1. BSR Dynamics at the Active Seepage Zone

Active seepage along Vestnesa Ridge has been documented at a few discrete sites at ~500 m wide pockmarks on the eastern Vestnesa Ridge segment (Figure 2), where gas chimneys associated with tectonic faults provide the pathways for fluid migration to the seafloor [*Bünz et al*., 2012; *Plaza-Faverola et al*., 2015]. In areas of focused fluid migration from greater depth, geothermal gradients are expected to be modified by increased heat flux, resulting in a shallower BSR and hence a thinner GHSZ [*Liu and Flemings*, 2007]. Such a dynamic response of the BSR to heat flow from depth has been documented from several margins [e.g., *Hornbach et al*., 2012; *Mann and Kukowski*, 1999; *Vadakkepuliyambatta et al*., 2015]. Along Vestnesa Ridge, the BSR shoaling in the active seepage region does not seem to be pronounced, though a relative shoaling with respect to the BSR at the inactive seepage region can be recognized. This relative shoaling of the BSR is best illustrated by comparison with the best fitting model (i.e., GC19; Figures 5f and 6). The BSR is slightly shallower (i.e., within the uncertainty range of the models) with respect to the GC19 model at the active seepage zone (Figure 6a). However, the same model underestimates the BSR depth elsewhere along Vestnesa Ridge, including inactive seep locations where evidence for past seepage activity exist (Figures 6c and 6d). Since the relative BSR shoaling is within the uncertainty range and considering the possibility of a deeper BSR due to unaccounted slightly higher *Vp*, it is difficult to further analyze the effect of heat flow on the BSR dynamics. Nonetheless, seepage in this part of Vestnesa Ridge indicates that anomalous heat flux from deeper formations has an effect on the BSR dynamics, potentially overshadowing the effect of other mechanisms determining its depth.

5.2. BSR Dynamics at Zones of Past Seepage Activity

Gas bubble release into the water column has not been identified toward the western segment of Vestnesa Ridge during numerous cruises to the area, and this region is thus referred to as inactive (Figure 2). In contrast to the observations at the active seepage region, the comparison between modeled and observed BSR does not indicate shoaling in response to anomalous high heat flow (Figure 5). The only indication of a potentially higher heat flow zone is at a chimney cluster associated with an outcropping fault where the GC19 model locally fits the BSR despite a clear trend of a BSR deeper than predicted in the surroundings (Figure 6c). This part of the ridge is thus ideal to constrain the impact of additional temperature and pressure related factors on the modeling results.

5.2.1. BSR Adjustment to Postglacial Pressure and Temperature Conditions

Our models assume that the BSR is at present-day steady state. However, competing processes such as sea level and temperature changes since the Last Glacial Maximum (LGM; >17,000 years ago) [*Rasmussen et al*., 2007; *Sztybor and Rasmussen*, 2016] may have an influence on the BSR dynamics. Increasing bottom water temperature-driven BSR readjustment shifts the BSR upward and in opposite direction to an adjustment in response to increased pressure. In a crude balance, a −1°C change in bottom water temperature and −100 m of water column with respect to present-day conditions (i.e., water depth >1000 m) would have shifted the BGHS +10 m and −10 m, respectively. These processes occur at a rate of a few millimeters per year and have a balancing effect [*Ruppel*, 1997]. Thus, climate-

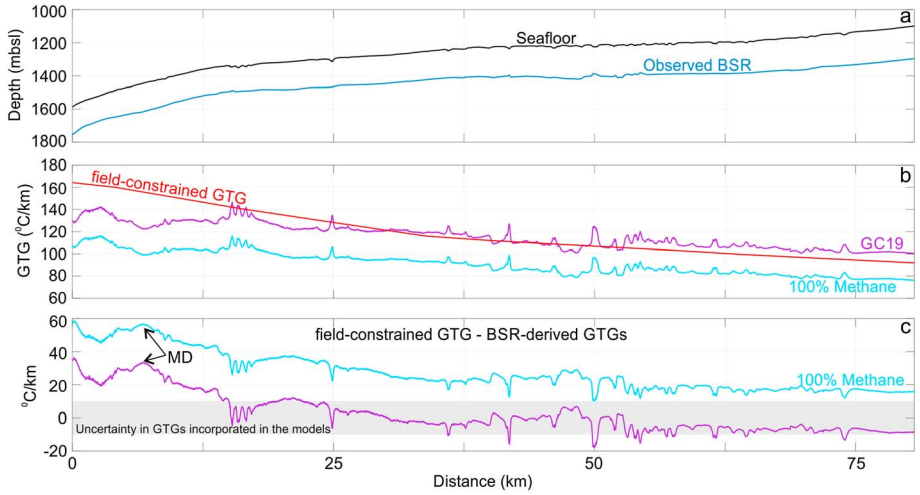

Figure 7. (a) Seafloor and observed BSR depth below sea level. (b) Comparison between shallow geothermal gradients (GTG) constrained from regional measurements (red) and predicted GTG from the BSR depth for GC19 composition (purple) and pure methane (blue). Except for the deepest part of the seismic data, shallow GTG measurements correlate well with GC19 BSR-predicted GTG. (c) Difference between the GTG used in our models and the GTG derived based on the BSR depth for GC19 (purple) and pure methane (blue); MD = maximum difference.

related pressure and temperature variations are not expected to have a significant impact on the BSR depth at present day along Vestnesa Ridge.

5.2.2. Overpressure Zones Beneath the BSR

The assumption of hydrostatic pressure in the models does not account for potential zones of overpressure at the BGHS. Pore fluid pressures in sedimentary basins with well-drained sediments are expected to remain hydrostatic down to ~2.5 km depth [*Gradmann and Beaumont*, 2012]. In the case of gas hydrate systems (i.e., commonly restricted to the upper 1 km of sediments) a hydrostatic pressure assumption through the sedimentary column is generally valid as long as zones of significantly reduced permeability prone to overpressure do not occur within the GHSZ [e.g., *Tinivella and Giustiniani*, 2013]. A pore fluid pressure higher than hydrostatic at the BGHS would shift the BSR downward. At Blake Ridge, a lithostatic gas pressure was identified at an interconnected free gas column immediately beneath the BGHS (Ocean Drilling Program (ODP) Site 997) [*Flemings et al*., 2003]. Gas input from deeper thermogenic gas reservoirs can promote overpressure buildup at interconnected gas columns beneath the BSR [*Flemings et al*., 2003; *Hornbach et al*., 2004]. By analogy with Blake Ridge, Vestnesa Ridge gas hydrate system may present overpressure conditions driven by the gas input from deep sediments, increased sedimentation rates, and tectonic stress distribution [*Plaza-Faverola et al*., 2015]. However, based on modeling results, the effect of overpressure on the BSR dynamics is assumed negligible at settings like Vestnesa Ridge (i.e., water depth >1000 m, bottom water temperatures <0°C, geothermal gradients >40°C km^{-1}, and presence of thermogenic gases) [*Tinivella and Giustiniani*, 2013]. Indeed, for a bulk density of 1500 kg m^{-3} through the upper 200 m of sediments offshore west Svalbard (i.e., as constrained from ODP Site 909) [*Myhre et al*., 1995], lithostatic pressure at the BGHS along Vestnesa Ridge would be 0.6–0.9 MPa higher than hydrostatic pressure. This would be equivalent to additional 70–90 m of water column height for the hydrostatic pressure approach, which in this setting would result in a BSR depth <10 m deeper than predicted for a purely hydrostatic approach. Occurrence of non-hydrostatic pressures in places would still be insufficient to explain the observed mismatch (i.e., >30 m in places) between observed BSR depths and predictions for constrained gas compositions (Figure 5).

5.2.3. Overestimation of the Geothermal Gradient

A modeled BGHS shallower than the observed BSR can be discussed in terms of how accurate is our approximation of the thermal regime in the shallow sediments. In general, the observed BSR depths indicate that the GTGs used in our models are too high. The BSR predicts significant spatial and sometimes localized variations of geothermal gradients, which are not anticipated by regional temperature measurements from seafloor probes (Figure 7). For example, to fit the observed BSR at the location of the largest misfit, the GTG has to be 123°C km^{-1} and 100°C km^{-1} for the GC19 composition and pure methane respectively (i.e., 35–55°C km^{-1} less than the value used in our models; Figures 7b and 7c). The

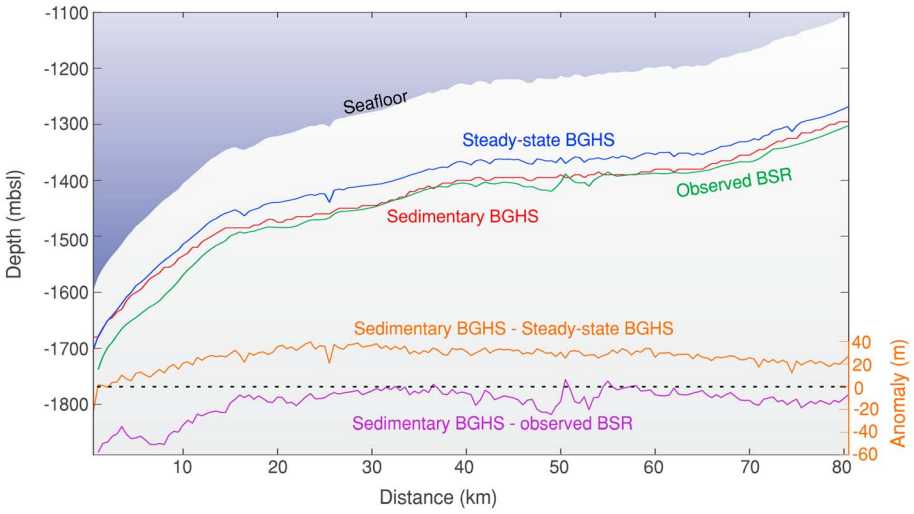

Figure 8. Two-dimensional profile along Vestnesa Ridge showing the effect of sedimentation on the BSR dynamics. The sediment temperature after accounting for the effect of sedimentation was estimated using numerical models for purely diffusive heat transport (supporting information Figures S2–S4). The base of gas hydrate stability (BGHS) was recalculated for the non-steady-state temperatures. The assumed steady state BGHS for pure methane can be 7–40 m shallower than the BGHS after accounting for sedimentation (sedimentary BGHS). Toward the westernmost part of the ridge, where the BSR inflection is most significant, sedimentation rates are lowest and the assumed steady state and sedimentary BGHS are comparable.

BSR predicts a westward increase by up to 20°C km^{-1} within 15 km from this location, which is a closer approximation to the >150°C km^{-1} value constrained by seafloor temperature probes (Figure 7c). A hypothetical GTG overestimation cannot be fully attributed to instrumental uncertainties. Therefore, we discuss potential explanations for cooler temperatures at the BSR than expected from background GTG values.

The temperature probes used to constrain GTG along Vestensa Ridge are located within few meters to kilometers away from our seismic profile (Figure 1). An interpolation from a temperature probe located over, e.g., a fault, may measure higher temperatures than at a location 10 km away from the fault. In addition, the assumption of constant thermal conductivities in estimating GTG from shallow (<10 m) temperature measurements could result in an overestimation compared to GTG estimated using deeper temperature measurements [*Stranne and O'Regan*, 2016]. Hypothetically, the BSR-derived GTG values predict either less heat flow than assumed by our models or a thermal conductivity that increases with depth within the GHSZ.

More fundamentally, the temperatures predicted by the BSR depth could be cooler than predicted from the background GTG if the basin's geothermal regime is still adjusting to newly deposited sediments [e.g., *Palumbo et al*., 1999; *Turcotte and Ahern*, 1977]. The crustal heat is constantly redistributed and the geotherms in newly deposited strata equilibrate toward warmer or cooler temperatures through time following deposition or erosion, respectively. Several studies have used analytical heat transport models to show that sedimentation and erosion can significantly affect the BSR depth [e.g., *Henrys et al*., 2003; *Hornbach et al*., 2008; *Martin et al*., 2004]. However, this is a complex problem that is commonly simplified by assuming that (1) the temperature was in steady state at the start time of the model and the background GTG is known, (2) the sedimentation/erosion rates have been consistently sustained through long intervals (millions of years) during basin evolution, and (3) the effect of compaction and basin subsidence has a negligible impact on the process of heat transfer through the sediments.

At Vestnesa Ridge, we lack constraints on the total sedimentary thickness and sedimentation rates to resolve the thermal evolution since the beginning of deposition ~19 Ma ago. Sedimentation rates have been estimated for three chronological markers (i.e., 0.2, 1.5, and 2.7 Ma) based on foraminifera analyses and seismic stratigraphy [*Consolaro et al*., 2015; *Plaza-Faverola et al*., 2015; *Sztybor and Rasmussen*, 2016]. Thus, to provide a physical sense of the potential effect of sedimentation on the BSR depth, we assume that the sediment temperature was at steady state condition prior to the onset of glaciations, 2.7 Ma ago. We ran a 2-D numerical model for purely diffusive heat transport in the sediments and recalculate the BGHS for the

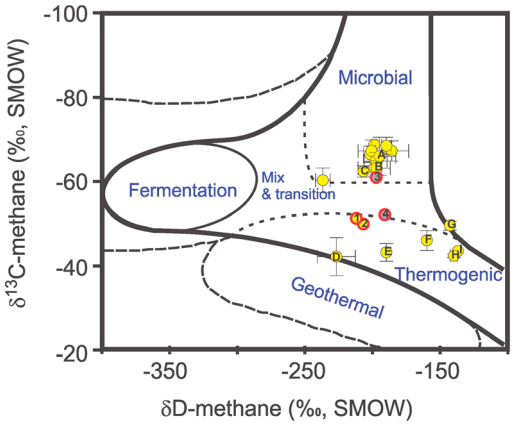

Figure 9. δ13C versus δD (deuterium) of CH4 diagram (modified from *Whiticar* [1999]) showing the thermogenic signature of gas samples from gas hydrates (GH; 1 and 2) and from headspace (3 and 4) gas samples on Vestnesa Ridge (red circles). Isotope values are presented in supporting information Table S1. Gas samples from other stratigraphic and structurally controlled gas hydrate provinces around the globe are also included for comparison [*Milkov*, 2005, and references therein]: A = Hydrate Ridge; B = Ulleung Basin; C = Offshore Sakhalin Island; D = Mackenzie Delta; E = Gulf of Mexico-Green Canyon; F = Gulf of Mexico-Mississippi; G = Gulf of Mexico-Atwater; H = Offshore Vancouver Island (Barkley Canyon); and I = Offshore Costa Rica.

non-steady-state temperatures (supporting information Figures S2–S4) [*Allen and Allen*, 2013; *Gerya*, 2010]. This modeling exercise results in a BGHS (i.e., referred to as sedimentary BGHS in Figure 8) that is approximately 7–40 m deeper than the assumed steady-state BGHS at the zones of minimum and maximum sedimentation rates, respectively (Figure 8). The relaxation time of the geotherms after sustained sedimentation for 1 Ma can be as long as 0.5 Ma. Whether the sediment temperature was at steady state at 2.7 Ma or has ever reached a steady state condition since the beginning of deposition cannot be resolved with the currently available data.

Interestingly, the largest anomaly in the BSR depth (i.e., up to 60 m with respect to the pure methane model) is exhibited within the westernmost 20 km where average sedimentation rates are lowest over the last ~2.7 Ma (Figures 3, 5a, and S3). We thus observe an effect of sedimentation on the BSR dynamics along Vestnesa Ridge that is overshadowed by additional processes, i.e., particularly at the zone of less sedimentation and maximum BSR deflection toward the mid-ocean ridge (Figures 8 and S3). Conjectural low GTGs with respect to background GTG toward the western tip of Vestnesa Ridge may be caused by crustal mid-ocean ridge processes, e.g., water percolation and localized cooling of the crust [*Davis et al.*, 1989]. Near-surface GTG values may not be providing an ideal constraint to the temperatures at the BSR depth. A GTG constrained over larger depth ranges would be a better approximation of the background GTG in the basin. Nevertheless, the westward decrease of the BSR depth despite an evident increase in hydrostatic pressure and decrease in sedimentation rates suggests that the BSR depth is somewhat consistent with the regionally constrained GTG values used in our models (Figures 3, 7, and 8).

5.3. Effect of Higher-Order Hydrocarbons on BSR Dynamics

The analysis above suggests that even after consideration of pressure and temperature instabilities within the GHSZ the mismatch between modeled and observed BSR is still unresolved. We take now into consideration the composition of the host gases in hydrates. Measured gas compositions from gravity cores (Table 1) reflect a spatial variability in the composition and the sources of gas along the ridge. The gas composition varies considerably within a small spatial range. We find that only small changes in the amount of propane (GC19 and GC04; Table 1) can cause significant variations in the predicted BGHS (Figure 5). We suggest that a deeper BSR than predicted along Vestnesa Ridge may reflect an input of thermogenic gas sources with significant amount of higher-order hydrocarbons (C_2, C_3, and higher) into the GHSZ. Such input of thermogenic gas is only partially reflected by the shallow headspace gas samples from the gravity cores due to the technical difficulties during sampling. In general, it is difficult to constrain the in situ gas composition from headspace gas samples taken at atmospheric pressure due to the degassing of samples upon core recovery. The presence of >5% ethane and other higher-order hydrocarbons as well as methane carbon isotopic ratios of ~40 ‰ point toward a significant contribution of thermogenic gas sources at Vestnesa Ridge (Figure 9) [*Paull and Ussler*, 2001]. Even with the abundant C_2+ measured though, these samples collected near the seafloor (<6 m bsf) along Vestnesa Ridge (Table 1) are likely to underestimate the contribution of higher-order hydrocarbons in the hydrate system at greater depths (within 140–190 m bsf), as recently documented from borehole data at the margins of Borneo [*Paganoni et al.*, 2016].

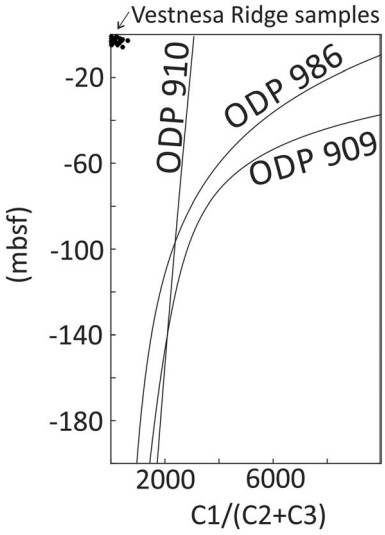

Figure 10. Plot of C1/(C2 + C3) ratios versus depth, documenting a decrease of microbial gas and increase of thermogenic gas with depth at the location of ocean drilling project (ODP) Sites 910, 986, and 909. The Vestnesa Ridge gravity core samples have C1/(C2 + C3) ratios <200, indicating a dominant thermogenic gas source near the seafloor.

Microbial gas sources show C_1/C_{2+} ratios typically greater than 1000, while for thermogenic gas this ratio is typically <100 (e.g., <50 at Green Canyon) [*Brooks et al.*, 1994]. Data from ODP-Sites 909, 911, and 986 surrounding Vestnesa Ridge [*Myhre et al.*, 1995] show that at regions without a proven hydrate system the C_1/C_{2+} ratio decreases from >2000 for the upper 60 m bsf to <1000 below the regional BSR depth (Figure 10). The ratio for our gas analyses is below 200 (Figure 10), consistent with thermogenic gas reaching the seafloor. Methane to ethane and heavier hydrocarbon ratios (C_1/C_{2+}) from drilling sites at other continental margins also reconcile the observations offshore west Svalbard, showing a general trend toward lower ratios with depth even in areas where a thermogenic gas source has not been anticipated [*Choi et al.*, 2013; *Kastner et al.*, 1998; *Lorenson et al.*, 2008; *Myhre et al.*, 1995; *Paull and Ussler*, 2001; *Trehu et al.*, 2004]. All these observations support our inference of larger amounts of higher-order hydrocarbons at depth that may enhance hydrate stability and widen the GHSZ.

In the context of leaking hydrocarbon provinces our analysis suggests that spatial BSR depth variations along Vestnesa Ridge may be explained reasonably well by modifying the gas compositions (e.g., by ~2% increase in C_2 and C_3 concentrations measured at GC19) with the exception of the zone of BSR inflection and maximum misfit (Figure 7c). A slightly deeper BSR at this location and its anomalous inflection remains puzzling but can be partially explained by the added effect of all the factors discussed.

5.4. Implications for Global Estimates of Carbons in Marine Gas Hydrates

Two main variables in estimating carbon in gas hydrates are the volume of pore space available for hydrate formation and the gas composition in the hydrate phase [*Dickens*, 2011; *Wallmann et al.*, 2012]. These two variables can be better constrained in stratigraphic gas hydrate accumulations (e.g., Blake Ridge [*Paull et al.*, 1996], Gulf of Mexico minibasins [*Milkov and Sassen*, 2002], the Ulleung Basin [*Choi et al.*, 2013], and Nankai Trough [*Matsumoto et al.*, 2004]) where microbial methane (i.e., formed in situ or supplied from shallow depth to the surface) is the dominant source of gas to form hydrates [e.g., *Dickens*, 2011; *Milkov and Sassen*, 2002; *Wallmann et al.*, 2012; *Xu and Ruppel*, 1999]. An additional effort is, however, required for constraining the GHSZ volume at structurally controlled hydrate systems where gas migration from deeper hydrocarbon reservoirs may result in a mixed gas source making the BSR more dynamic [e.g., *Marín-Moreno et al.*, 2013; *Wallmann et al.*, 2012]. New structurally controlled hydrate systems are constantly identified worldwide that show mixed gas compositions and highly depleted methane carbon isotopes (Figure 8).

Our study at Vestnesa Ridge shows that from the geochemistry perspective, gas hydrate stability modeling assuming pure methane may represent a significant underestimation, by up to 60 m, of the GHSZ thickness. Similarly, modeling the base of gas hydrate stability with constrains from gravity core gas compositions—not necessarily representative of gas compositions at greater depths—may still represent a significant underestimation by 20–60 m of the GHSZ thickness. For comparison, the GHSZ thickness constrained for deeper (>6 m) thermogenic gas samples at the northern Gulf of Mexico hydrate province results in a 60% thicker GHSZ (i.e., in a setting where the GHSZ is >400 m thick) with respect to the pure methane GHSZ thickness [*Milkov and Sassen*, 2000].

Structurally controlled gas hydrate systems—characterized by high fluid fluxes—have a larger potential for high amounts of gas hydrate accumulations if compared to stratigraphic provinces [*Milkov and Sassen*, 2002, and references therein]. Large structural gas hydrate accumulations, presumably hosting significant but yet unidentified amounts of thermogenic gas hydrates, may exist in margins with proven petroleum systems (e.g., the Hikurangi Margin with ~40,000 km^2 of mapped BSR) [*Henrys et al*., 2003].

The volume of the GHSZ and the amount of carbon trapped in hydrates will be larger in thermogenic hydrate systems where ethane, propane, and butane are part of the hydrate structure. To illustrate the above we assume the following: (1) an area of ~4000 km^2 based on picked BSR in the region [*Sarkar et al*., 2012] and a GHSZ volume of ~700 km^3 (supporting information Figures S2 and S5); (2) a maximum gas hydrate saturation of 3% of the total GHSZ volume [*Hustoft et al*., 2009], (3) a 94% cage occupancy by gas in hydrates [*Lorenson and Collett*, 2000], (4) 1 m thick sulfate-methane transition zone where gas hydrates are not expected to form [*Hong et al*., 2016], and (5) the equilibrium gas composition in the hydrate phase for gas samples in core GC19 (i.e., C_1 = 0.7508, C_2 = 0.02, C_3 = 0.1232, iC_4 = 0.1054, and nC_4 = 0.0006). For the assumed gas composition in the hydrate phase (type II gas hydrates) Vestnesa Ridge would host 2.88 Gt of carbon, while the total amount of carbon would be 1.82 Gt if we consider the pure methane scenario. For the BSR area considered by *Hustoft et al*. [2009], their estimate of 0.52 Gt of carbons assuming pure methane becomes 0.83 Gt of carbons considering the hydrate phase equivalent to gas concentrations from GC19.

Similarly, if extrapolated to other Arctic regions where major petroleum provinces are known to exist, a similar gas concentration assumed in the gas hydrate phase would transform the 9000 Gt of carbons estimated by *Biastoch et al*. [2011] into 14,260 Gt. This difference is in turn about 10 times the upper boundary in the Arctic carbon inventory estimated by *Marín-Moreno et al*. [2016] (i.e., ~541 Gt).

Estimates of the global and Arctic carbon inventory based on different approaches remain highly divergent [*Biastoch et al*., 2011; *Kretschmer et al*., 2015; *Marín-Moreno et al*., 2016; *Moridis et al*., 2013]. Observations from Vestnesa Ridge highlight the importance of geochemically and geothermally constrained field predictions of the GHSZ thickness. Such predictions may result not only in the identification of hidden thermogenic gas hydrate accumulations but also in a refined carbon inventory within thermogenic gas hydrate systems.

6. Conclusions

An integrated analysis of seismic and geochemical data from Vestnesa Ridge gas hydrate system provides insight into the dynamics of a structurally controlled gas hydrate system adjacent to mid-ocean ridges. Assuming that the bottom-simulating reflector (BSR) marks the base of the gas hydrate stability zone in this structurally controlled fluid flow system, field-constrained gas hydrate stability modeling leads to the following main conclusions:

1. The observed BSR along >100 km long Vestnesa sedimentary ridge is tens of meters deeper than predicted assuming steady state conditions for pure methane hydrates as well as for constrained headspace thermogenic gas compositions from gravity cores. The magnitude of the misfit between the observed BSR and the models varies spatially reflecting the importance of different mechanisms controlling BSR dynamics depending on the pattern of seepage activity.
2. The BSR at the region of active seepage is affected by the inflow of warmer fluids carrying gases from deeper reservoirs, showing a relative shoaling of the BSR, possibly overshadowing the effect of additional processes on the BSR dynamics. In contrast, zones with evidence of past seepage (inactive pockmarks), allowed studying the potential effect of additional processes on the BSR dynamics related to the pressure, thermal, and geochemical regimes of the basin.
3. While the observed BSR anomalies cannot be explained by pressure-related processes, spatial and temporal variations in the geothermal regime may be having a considerable effect on the BSR dynamics. Sedimentary deposition and mid-ocean ridge crustal processes could lead to unexpectedly lower geothermal gradients than constrained by near-seafloor temperature probes.
4. Similarly, spatial variations in gas compositions within the gas hydrate stability zone provide a plausible explanation for a deeper BSR than predicted. Measured gas compositions from the upper few meters of sediments most likely do not correctly represent, but underestimate, the amount of thermogenic gas present within the deeper gas hydrate system.

5. Finally, an assumption of constant gas composition (i.e., pure methane) within the entire gas hydrate stability zone may leave thermogenic gas hydrate accumulations unidentified. When placed in a global context, the presented investigations along Vestnesa Ridge emphasizes the importance of constraining thermogenic gas hydrate accumulations and the nature of the gas deeper in the hydrate system, in the refinement of the global gas hydrate inventory and amount of carbon stored in gas hydrates.

Acknowledgments
This research is part of the Centre for Arctic Gas Hydrate, Environment and Climate and was supported by the Research Council of Norway through its Centers of Excellence funding scheme grant 223259. Jens Greinert contribution was partially supported by COST Action PERGAMON (ESSEM 0902). Special thanks to the crew of R/V *Helmer Hanssen* for support with data acquisition and the group of Mark Schmidt at GEOMAR for support with processing of geochemical samples. Two anonymous reviewers provided valuable comments that resulted in significant improvements. We are thankful to Matthew Hornbach for insightful discussions about heat transport in the sediments. The data are stored at CAGE's data repository and are accessible by contacting the corresponding author.

References

Allen, P. A., and J. R. Allen (2013), *Basin Analysis: Principles and Application to Petroleum Play Assessment*, 3rd ed., pp. 37–39, John Wiley, Hoboken, N. J.

Bale, S., T. M. Alves, and G. F. Moore (2014), Distribution of gas hydrates on continental margins by means of a mathematical envelope: A method applied to the interpretation of 3D seismic data, *Geochem. Geophys. Geosyst.*, *15*, 52–68, doi:10.1002/2013GC004938.

Berndt, C., T. Feseker, T. Treude, S. Krastel, V. Liebetrau, H. Niemann, V. J. Bertics, I. Dumke, K. Dünnbier, and B. Ferré (2014), Temporal constraints on hydrate-controlled methane seepage off Svalbard, *Science*, *343*(6168), 284–287.

Biastoch, A., et al. (2011), Rising Arctic Ocean temperatures cause gas hydrate destabilization and ocean acidification, *Geophys. Res. Lett.*, *38*, L08602, doi:10.1029/2011GL047222.

Brooks, J., M. Kennicutt, R. Fay, T. McDonald, and R. Sassen (1984), Thermogenic gas hydrates in the Gulf of Mexico, *Science*, *225*(4660), 409–411.

Brooks, J. M., A. L. Anderson, R. Sassen, M. C. Kennicutt, and N. L. Guinasso (1994), Hydrate occurrences in shallow subsurface cores from continental slope sediments, *Ann. N. Y. Acad. Sci.*, *715*(1), 381–391.

Bünz, S., S. Polyanov, S. Vadakkepuliyambatta, C. Consolaro, and J. Mienert (2012), Active gas venting through hydrate-bearing sediments on the Vestnesa Ridge, offshore W-Svalbard, *Mar. Geol.*, *332–334*, 189–197, doi:10.1016/j.margeo.2012.09.012.

Chand, S., J. Mienert, K. Andreassen, J. Knies, L. Plassen, and B. Fotland (2008), Gas hydrate stability zone modelling in areas of salt tectonics and pockmarks of the Barents Sea suggests an active hydrocarbon venting system, *Mar. Pet. Geol.*, *25*(7), 625–636.

Choi, J., J.-H. Kim, M. E. Torres, W.-L. Hong, J.-W. Lee, B. Y. Yi, J.-J. Bahk, and K. E. Lee (2013), Gas origin and migration in the Ulleung Basin, East Sea: Results from the second Ulleung Basin gas hydrate drilling expedition (UBGH2), *Mar. Pet. Geol.*, *47*, 113–124.

Consolaro, C., T. Rasmussen, G. Panieri, J. Mienert, S. Bünz, and K. Sztybor (2015), Carbon isotope (δ13C) excursions suggest times of major methane release during the last 14 kyr in Fram Strait, the deep-water gateway to the Arctic, *Clim. Past*, *11*(4), 669–685.

Crane, K., E. Sundvor, R. Buck, and F. Martinez (1991), Rifting in the northern Norwegian-Greenland Sea: Thermal tests of asymmetric spreading, *J. Geophys. Res.*, *96*(B9), 14,529–14,550.

Davis, E. E., D. S. Chapman, C. B. Forster, and H. Villinger (1989), Heat-flow variations correlated with buried basement topography on the Juan de Fuca Ridge flank, *Nature*, *342*(6249), 533–537.

Dickens, G. R. (2011), Down the rabbit hole: Toward appropriate discussion of methane release from gas hydrate systems during the Paleocene-Eocene thermal maximum and other past hyperthermal events, *Clim. Past*, *7*(3), 831–846.

Dickens, G. R., and M. S. Quinby-Hunt (1994), Methane hydrate stability in seawater, *Geophys. Res. Lett.*, *21*, 2115–2118, doi:10.1029/94GL01858.

Dobrynin, V. (1981), Gas hydrates—A possible energy resources, *Long-Term Energy Resour.*, *1*, 727–729.

Dumke, I., E. B. Burwicz, C. Berndt, D. Klaeschen, T. Feseker, W. H. Geissler, and S. Sarkar (2016), Gas hydrate distribution and hydrocarbon maturation north of the Knipovich Ridge, western Svalbard margin, *J. Geophys. Res. Solid Earth*, *121*, 1405–1424, doi:10.1002/2015JB012083.

Eiken, O., and K. Hinz (1993), Contourites in the Fram Strait, *Sediment. Geol.*, *82*(1), 15–32.

Engen, Ø., J. I. Faleide, and T. K. Dyreng (2008), Opening of the Fram Strait gateway: A review of plate tectonic constraints, *Tectonophysics*, *450*(1), 51–69.

Flemings, P. B., X. L. Liu, and W. J. Winters (2003), Critical pressure and multiphase flow in Blake Ridge gas hydrates, *Geology*, *31*(12), 1057–1060.

Gerya, T. (2010), *Introduction to Numerical Geodynamic Modelling*, pp. 133–146, Cambridge Univ. Press, Cambridge, U. K.

Ginsburg, G., R. Guseynov, A. Dadashev, G. Ivanova, S. Kazantsev, V. Solov'yev, E. Telepnev, R. Y. Askeri-Nasirov, A. Yesikov, and V. Mal'tseva (1992), Gas hydrates of the southern Caspian, *Int. Geol. Rev.*, *34*(8), 765–782.

Goswami, B. K., K. A. Weitemeyer, T. A. Minshull, M. C. Sinha, G. K. Westbrook, A. Chabert, T. J. Henstock, and S. Ker (2015), A joint electromagnetic and seismic study of an active pockmark within the hydrate stability field at the Vestnesa Ridge, west Svalbard margin, *J. Geophys. Res. Solid Earth*, *120*, 6797–6822, doi:10.1002/2015JB012344.

Gradmann, S., and C. Beaumont (2012), Coupled fluid flow and sediment deformation in margin-scale salt-tectonic systems: 2. Layered sediment models and application to the northwestern Gulf of Mexico, *Tectonics*, *31*, TC4011, doi:10.1029/2011TC003035.

Haacke, R. R., G. K. Westbrook, and M. S. Riley (2008), Controls on the formation and stability of gas hydrate-related bottom-simulating reflectors (BSRs): A case study from the west Svalbard continental slope, *J. Geophys. Res.*, *113*, B05104, doi:10.1029/2007JB005200.

Henrys, S. A., S. Ellis, and C. Uruski (2003), Conductive heat flow variations from bottom-simulating reflectors on the Hikurangi Margin, New Zealand, *Geophys. Res. Lett.*, *30*(2), 1065, doi:10.1029/2002GL015772.

Hong, W. L., S. Sauer, G. Panieri, W. G. Ambrose, R. H. James, A. Plaza-Faverola, and A. Schneider (2016), Removal of methane through hydrological, microbial, and geochemical processes in the shallow sediments of pockmarks along eastern Vestnesa Ridge (Svalbard), *Limnol. Oceanogr.*, doi:10.1002/lno.10299.

Hornbach, M. J., N. L. Bangs, and C. Berndt (2012), Detecting hydrate and fluid flow from bottom simulating reflector depth anomalies, *Geology*, *40*(3), 227–230.

Hornbach, M. J., D. M. Saffer, and W. S. Holbrook (2004), Critically pressured free-gas reservoirs below gas-hydrate provinces, *Nature*, *427*(6970), 142–144, doi:10.1038/nature02172.

Hornbach, M. J., D. M. Saffer, W. S. Holbrook, H. J. A. Van Avendonk, and A. R. Gorman (2008), Three-dimensional seismic imaging of the Blake Ridge methane hydrate province: Evidence for large, concentrated zones of gas hydrate and morphologically driven advection, *J. Geophys. Res.*, *113*, B07101, doi:10.1029/2007JB005392.

Hustoft, S., S. Bunz, J. Mienert, and S. Chand (2009), Gas hydrate reservoir and active methane-venting province in sediments on $<$20 Ma young oceanic crust in the Fram Strait, offshore NW-Svalbard, *Earth Planet. Sci. Lett.*, *284*(1–2), 12–24, doi:10.1016/j.epsl.2009.03.038.

Johnson, J. E., J. Mienert, A. Plaza-Faverola, S. Vadakkepuliyambatta, J. Knies, S. Bünz, K. Andreassen, and B. Ferré (2015), Abiotic methane from ultraslow-spreading ridges can charge Arctic gas hydrates, *Geology*, *45*, 36441, doi:10.1130/G36440.1.

Kastner, M., K. A. Kvenvolden, and T. D. Lorenson (1998), Chemistry, isotopic composition, and origin of a methane-hydrogen sulfide hydrate at the Cascadia subduction zone, *Earth Planet. Sci. Lett.*, *156*(3), 173–183.
Khlystov, O., M. De Batist, H. Shoji, A. Hachikubo, S. Nishio, L. Naudts, J. Poort, A. Khabuev, O. Belousov, and A. Manakov (2013), Gas hydrate of Lake Baikal: Discovery and varieties, *J. Asian Earth Sci.*, *62*, 162–166.
Kinoshita, M., G. F. Moore, and Y. N. Kido (2011), Heat flow estimated from BSR and IODP borehole data: Implication of recent uplift and erosion of the imbricate thrust zone in the Nankai Trough off Kumano, *Geochem. Geophys. Geosyst.*, *12*, Q0AD18, doi:10.1029/2011GC003609.
Klauda, J. B., and S. I. Sandler (2005), Global distribution of methane hydrate in ocean sediment, *Energy Fuels*, *19*(2), 459–470.
Kretschmer, K., A. Biastoch, L. Rüpke, and E. Burwicz (2015), Modeling the fate of methane hydrates under global warming, *Global Biogeochem. Cycles*, *29*, 610–625, doi:10.1002/2014GB005011.
Kvenvolden, K. A., and G. E. Claypool (1988), *Gas Hydrates in Oceanic Sediment*, pp. 18–33, Dep. of the Inter., U.S. Geol. Surv., Menlo Park, Calif.
Kvenvolden, K. A., and M. E. Field (1981), Thermogenic hydrocarbons in unconsolidated sediment of Eel River basin, offshore northern California: GEOLOGIC NOTES, *AAPG Bull.*, *65*(9), 1642–1646.
Kvenvolden, K. A., and T. D. Lorenson (2001), The global occurrence of natural gas hydrate, *Geophys. Monogr.*, *124*, 3–18.
Liu, X., and P. B. Flemings (2011), Capillary effects on hydrate stability in marine sediments, *J. Geophys. Res.*, *116*, B07102, doi:10.1029/2010JB008143.
Liu, X. L., and P. B. Flemings (2007), Dynamic multiphase flow model of hydrate formation in marine sediments, *J. Geophys. Res.*, *112*, B03101, doi:10.1029/2005JB004227.
Lorenson, T. D., and T. S. Collett (2000), Gas content and composition of gas hydrate from sediments of the southeastern North American continental margin, paper presented at Proceedings of the Ocean Drilling Program, Scientific Results.
Lorenson, T. D., G. E. Claypool, and J. A. Dougherty (2008), Natural gas geochemistry of sediments drilled on the 2005 Gulf of Mexico JIP cruise, *Mar. Pet. Geol.*, *25*(9), 873–883.
Lu, H., Y. Seo, J. Lee, I. Moudrakovski, J. A. Ripmeester, N. R. Chapman, R. B. Coffin, G. Gardner, and J. Pohlman (2007), Complex gas hydrate from the Cascadia margin, *Nature*, *445*(7125), 303–306.
Lu, Z., and N. Sultan (2008), Empirical expressions for gas hydrate stability law, its volume fraction and mass-density at temperatures 273.15 K to 290.15 K, *Geochem. J.*, *42*(2), 163–175.
MacKay, M. E., R. D. Jarrard, G. K. Westbrook, and R. D. Hyndman (1995), The Shipboard Scientific Party, Leg 146, 1995. Origin of bottom-simulating reflectors: Geophysical evidence from the Cascadia accretionary prism, *Geology*, *22*, 459–462.
Mann, D., and N. Kukowski (1999), Numerical modelling of focussed fluid flow in the Cascadia accretionary wedge, *J. Geodyn.*, *27*(3), 359–372.
Marín-Moreno, H., T. A. Minshull, G. K. Westbrook, B. Sinha, and S. Sarkar (2013), The response of methane hydrate beneath the seabed offshore Svalbard to ocean warming during the next three centuries, *Geophys. Res. Lett.*, *40*, 5159–5163, doi:10.1002/grl.50985.
Marín-Moreno, H., M. Giustiniani, U. Tinivella, and E. Piñero (2016), The challenges of quantifying the carbon stored in Arctic marine gas hydrate, *Mar. Pet. Geol.*, *71*, 76–82, doi:10.1016/j.marpetgeo.2015.11.014.
Martin, V., P. Henry, H. Nouze, M. Noble, J. Ashi, and G. Pascal (2004), Erosion and sedimentation as processes controlling the BSR-derived heat flow on the eastern Nankai margin, *Earth Planet. Sci. Lett.*, *222*(1), 131–144.
Matsumoto, R., H. Tomaru, and H. Lu (2004), Detection and evaluation of gas hydrates in the eastern Nankai Trough by geochemical and geophysical methods, *Resour. Geol.*, *54*(1), 53–67.
Mattingsdal, R., J. Knies, K. Andreassen, K. Fabian, K. Husum, K. Grøsfjeld, and S. De Schepper (2014), A new 6 Myr stratigraphic framework for the Atlantic–Arctic gateway, *Quat. Sci. Rev.*, *92*, 170–178.
Mienert, J., and S. Bünz (2016), Bottom simulating seismic reflectors (BSR), in *Encyclopedia of Marine Geosciences*, edited by J. Harff et al., pp. 62–67, Springer, Berlin.
Mienert, J., S. Bunz, S. Guidard, M. Vanneste, and C. Berndt (2005), Ocean bottom seismometer investigations in the Ormen Lange area offshore mid-Norway provide evidence for shallow gas layers in subsurface sediments, *Mar. Pet. Geol.*, *22*(1–2), 287–297, doi:10.1016/j.marpetgeo.2004.10.020.
Milkov, A. V. (2005), Molecular and stable isotope compositions of natural gas hydrates: A revised global dataset and basic interpretations in the context of geological settings, *Org. Geochem.*, *36*(5), 681–702.
Milkov, A. V., and R. Sassen (2000), Thickness of the gas hydrate stability zone, Gulf of Mexico continental slope, *Mar. Pet. Geol.*, *17*(9), 981–991.
Milkov, A. V., and R. Sassen (2002), Economic geology of offshore gas hydrate accumulations and provinces, *Mar. Pet. Geol.*, *19*(1), 1–11.
Moridis, G. J., T. S. Collett, R. Boswell, S. Hancock, J. Rutqvist, C. Santamarina, T. Kneafsey, M. T. Reagan, M. Pooladi-Darvish, and M. Kowalsky (2013), Gas hydrates as a potential energy source: State of knowledge and challenges, in *Advanced Biofuels and Bioproducts*, pp. 977–1033, Springer, New York.
Myhre, A. M., J. Thiede, J. V. Firth, and A. S. Party (1995), Proc. ODP, Init. Repts, 151: College Station, TX (Ocean Drilling Program).doi:10.2973/odp.proc.ir.151.1995.*Rep*.
National Oceanographic Data Center (2013), World Ocean database. [Available at http://www.nodc.noaa.gov/General/temperature.html), edited.]
Paganoni, M., J. Cartwright, M. Foschi, R. Shipp, and P. Van Rensbergen (2016), Structure II gas hydrates found below the bottom-simulating reflector, *Geophys. Res. Lett.*, *43*, 5696–5706, doi:10.1002/2016GL069452.
Palumbo, F., I. G. Main, and G. Zito (1999), The thermal evolution of sedimentary basins and its effect on the maturation of hydrocarbons, *Geophys. J. Int.*, *139*(1), 248–260.
Paull, C., R. Matsumoto, and P. Wallace (1996), The Leg 164 Scientific party, paper presented at Proceedings, ODP Initial Reports.
Paull, C. K., and W. Ussler (2001), History and significance of gas sampling during DSDP and ODP drilling associated with gas hydrates, in *Natural Gas Hydrates: Occurrence, Distribution, and Detection*, pp. 53–65, AGU, Washington, D. C., doi:10.1029/GM124p0053.
Pecher, I., S. Henrys, S. Ellis, S. Chiswell, and N. Kukowski (2005), Erosion of the seafloor at the top of the gas hydrate stability zone on the Hikurangi Margin, New Zealand, *Geophys. Res. Lett.*, *32*, L24603, doi:10.1029/2005GL024687.
Peszynska, M., W.-L. Hong, M. E. Torres, and J.-H. Kim (2016), Methane hydrate formation in Ulleung Basin under conditions of variable salinity: Reduced model and experiments, *Transp. Porous Media*, *114*(1), 1–27.
Petersen, C. J., S. Bünz, S. Hustoft, J. Mienert, and D. Klaeschen (2010), High-resolution P-Cable 3D seismic imaging of gas chimney structures in gas hydrated sediments of an Arctic sediment drift, *Mar. Pet. Geol.*, *27*(9), 1981–1994, doi:10.1016/j.marpetgeo.2010.06.006.
Pinero, E., C. Hensen, M. Haeckel, K. Wallmann, W. Rottke, T. Fuchs, and O. Schenk (2014), Gas hydrate accumulations at the Alaska north slope: Total assessment based on 3D petroleum system modeling, paper presented at Proceedings of the 8th International Conference on Gas Hydrates (ICGH8–2014), Beijing, China.
Planke, S., F. N. Eriksen, C. Berndt, J. Mienert, and D. Masson (2009), P-Cable high-resolution seismic, *Oceanography*, *22*(1), 85.

Plaza-Faverola, A., S. Bünz, J. E. Johnson, S. Chand, J. Knies, J. Mienert, and P. Franek (2015), Role of tectonic stress in seepage evolution along the gas hydrate-charged Vestnesa Ridge, Fram Strait, *Geophys. Res. Lett.*, *42*, 733–742, doi:10.1002/2014GL062474.

Rajan, A., J. Mienert, S. Bünz, and S. Chand (2012), Potential serpentinization, degassing, and gas hydrate formation at a young (<20 Ma) sedimented ocean crust of the Arctic Ocean ridge system, *J. Geophys. Res.*, *117*, B03102, doi:10.1029/2011JB008537.

Rasmussen, T. L., E. Thomsen, M. A. Ślubowska, S. Jessen, A. Solheim, and N. Koç (2007), Paleoceanographic evolution of the SW Svalbard margin (76°N) since 20,000 14 C yr BP, *Quatern. Res.*, *67*(1), 100–114.

Ruppel, C. (1997), Anomalously cold temperatures observed at the base of the gas hydrate stability zone on the US Atlantic passive margin, *Geology*, *25*(8), 699–702.

Sarkar, S., C. Berndt, T. A. Minshull, G. K. Westbrook, D. Klaeschen, D. G. Masson, A. Chabert, and K. E. Thatcher (2012), Seismic evidence for shallow gas-escape features associated with a retreating gas hydrate zone offshore west Svalbard, *J. Geophys. Res.*, *117*, B09102, doi:10.1029/2011JB009126.

Shipley, T. H., M. H. Houston, R. T. Buffler, F. J. Shaub, K. J. McMillen, J. W. Ladd, and J. L. Worzel (1979), Seismic evidence for widespread possible gas hydrate horizons on continental slopes and rises, *AAPG Bull.*, *63*(12), 2204–2213.

Skarke, A., C. Ruppel, M. Kodis, D. Brothers, and E. Lobecker (2014), Widespread methane leakage from the sea floor on the northern US Atlantic margin, *Nat. Geosci.*, *7*(9), 657–661, doi:10.1038/ngeo2232.

Sloan, E. D., and C. A. Koh (2008), *Clathrate Hydrates of Natural Gases*, 3rd ed., pp. 257–314, CRC Press, Boca Raton, Fla.

Smith, A. J., J. Mienert, S. Bünz, and J. Greinert (2014), Thermogenic methane injection via bubble transport into the upper Arctic Ocean from the hydrate-charged Vestnesa Ridge, Svalbard, *Geochem. Geophys. Geosyst.*, *15*, 1945–1959, doi:10.1002/2013GC005179.

Soloviev, V. (2002), Global estimation of gas content in submarine gas hydrate accumulations, *Geol. Geofiz.*, *43*(7), 648–661.

Stranne, C., and M. O'Regan (2016), Conductive heat flow and nonlinear geothermal gradients in marine sediments—Observations from Ocean Drilling Program boreholes, *Geo-Mar. Lett.*, *36*(1), 25–33.

Sultan, N., P. Cochonat, J.-P. Foucher, and J. Mienert (2004), Effect of gas hydrates melting on seafloor slope instability, *Mar. Geol.*, *213*(1), 379–401.

Sundvor, E., O. Eldholm, T. P. Gladczenko, and S. Planke (2000), Norwegian-Greenland Sea thermal field, *Geol. Soc. London, Spec. Publ.*, *167*(1), 397–410, doi:10.1144/gsl.sp.2000.167.01.15.

Sztybor, K., and T. L. Rasmussen (2016), Diagenetic disturbances of marine sedimentary records from methane-influenced environments in the Fram Strait as indications of variation in seep intensity during the last 35 000 years, *Boreas*, *46*, 212–228, doi:10.1111/bor.12202.

Tinivella, U., and M. Giustiniani (2013), Variations in BSR depth due to gas hydrate stability versus pore pressure, *Global Planet. Change*, *100*, 119–128.

Torres, M., A. M. Trehu, N. Cespedes, M. Kastner, U. Wortmann, J. H. Kim, P. Long, A. Malinverno, J. Pohlman, and M. Riedel (2008), Methane hydrate formation in turbidite sediments of northern Cascadia, IODP Expedition 311, *Earth Planet. Sci. Lett.*, *271*(1), 170–180.

Trehu, A. M., P. E. Long, M. Torres, G. Bohrmann, F. Rack, T. Collett, D. Goldberg, A. Milkov, M. Riedel, and P. Schultheiss (2004), Three-dimensional distribution of gas hydrate beneath southern hydrate ridge: Constraints from ODP Leg 204, *Earth Planet. Sci. Lett.*, *222*(3), 845–862.

Turcotte, D., and J. Ahern (1977), On the thermal and subsidence history of sedimentary basins, *J. Geophys. Res.*, *82*(26), 3762–3766.

Vadakkepuliyambatta, S., M. J. Hornbach, S. Bünz, and B. J. Phrampus (2015), Controls on gas hydrate system evolution in a region of active fluid flow in the SW Barents Sea, *Mar. Pet. Geol.*, *66*(Part 4), 861–872, doi:10.1016/j.marpetgeo.2015.07.023.

Vogt, P., J. Gardner, K. Crane, E. Sundvor, F. Bowles, and G. Cherkashev (1999), Ground-truthing 11-to 12-kHz side-scan sonar imagery in the Norwegia–Greenland Sea: Part I: Pockmarks on the Vestnesa Ridge and Storegga slide margin, *Geo Mar. Lett.*, *19*(1–2), 97–110.

Vogt, P. R., K. Crane, E. Sundvor, M. D. Max, and S. L. Pfirman (1994), Methane-generated (?) pockmarks on young, thickly sedimented oceanic crust in the Arctic: Vestnesa Ridge, Fram Strait, *Geology*, *22*(3), 255–258.

Wallmann, K., E. Pinero, E. Burwicz, M. Haeckel, C. Hensen, A. Dale, and L. Ruepke (2012), The global inventory of methane hydrate in marine sediments: A theoretical approach, *Energies*, *5*(7), 2449–2498.

Westbrook, G. K., et al. (2009), Escape of methane gas from the seabed along the West Spitsbergen continental margin, *Geophys. Res. Lett.*, *36*, L15608, doi:10.1029/2009GL039191.

Whiticar, M. J. (1999), Carbon and hydrogen isotope systematics of bacterial formation and oxidation of methane: *Chem. Geol.*, *161*(1–3), 291–314.

Xu, W., and C. Ruppel (1999), Predicting the occurrence, distribution, and evolution of methane gas hydrate in porous marine sediments, *J. Geophys. Res.*, *104*(B3), 5081–5095.